APPLICATION OF EULER METHOD TO TRANSONIC FLOW COMPUTATION OF A HYPERSONIC CONFIGURATION

Dennis B. Finley*
Lockheed Fort Worth Company
Fort Worth, TX 76101

Abstract

Results obtained with an Euler code (Hawk, a version of PARC3D) applied to a representative hypersonic vehicle at transonic conditions are evaluated. This method was found to provide good prediction of vehicle forces, including non-linear normal forces associated with upper-surface vortices. The creation of vorticity and upper-surface vortex lift from the inviscid Euler method is compared with results from a fully-viscous solution for the forebody of the configuration. The deviation between computational predictions and test results for overall forces are shown.

Introduction

Application of Euler solvers to vortex-dominated flows has shown the ability of the inviscid Euler equations to provide estimates of vortex structures due to the inclusion of rotational effects. In compressible flows the vorticity is generated from the entropy gradients through curved shocks [1]. Computational studies of sharp and blunt leading-edge delta[2-3] wings include characterization of the primary upper-surface rotational feature in the Euler results having outward displacement from the full-viscous primary vortex. The strong overexpansion to maintain attached flow creates higher levels of local vorticity than shown in the viscous results [4]. The secondary separation zone that is found in viscous calculation and experimental results from such geometries is not present in the Euler results. Applications of Navier-Stokes solvers on sharp tangent-ogive cylinders at angles of attack from 20 to 30 degrees indicated the influence of small surface geometry perturbations in the extreme nose region on vortex formation and interaction [5] and the significance of grid resolution on prediction of separation line modeling [6]. In viscous calculations at α/δ of 3 degrees, vortex structures on blunted cones were shown to be weaker, smaller in extent and spaced wider apart than corresponding sharp-cone vortices [7]. The hypersonic vehicle class of configurations generally exhibit large fuselages with relatively blunt leading edges, and small wings such that the general flow structure at transonic speeds is similar to forebody flows. In the current paper, the flow structure generated in the nose and forebody region by an Euler code is compared to Navier-Stokes results on the same geometry. Comparisons are also made between Euler calculations for the full hypersonic configuration and available test data to show the adequacy of Euler predictions for overall inviscid forces.

Flow Solver

The code used for the study was Hawk3D, a version of PARC3D [8] developed at LFWC. This code has a finite-difference formulation employing central differences. The Beam-Warming implicit scheme with approximate factorization is used for the solver. The code is shock-capturing. The governing equations are expressed as:

$$\frac{\partial}{\partial t}Q + \frac{\partial}{\partial X_j}F = \left(\frac{1}{Re}\right)\frac{\partial}{\partial X_j}G_j$$

where Q is a vector containing the conservation variables mass, momentum and energy:

$$Q = \begin{bmatrix} \rho \\ \rho u_i \\ E \end{bmatrix}$$

* Engineering Group Specialist, Senior Member AIAA

the F_j vectors contain the inviscid fluxes:

$$F_j = \begin{bmatrix} \rho u_j \\ \rho u_i u_j + P\delta_{ij} \\ (E+P)\,u_j \end{bmatrix}$$

where E is the total internal energy and P is pressure. The viscous flux terms (G_j) are put on the right-hand side:

$$G_j = \begin{bmatrix} 0 \\ \tau_{ij} \\ u_k \tau_{jk} - q_j \end{bmatrix}$$

The total energy per unit volume, E, is defined as:

$$E = \rho\left(e + (\frac{1}{2})\left(\sum_{j=1}^{3} u_j \times u_j\right)\right)$$

for the three dimensions. Modifications and enhancements to this code have been made by LFWC to improve application of the Baldwin-Lomax turbulence model, and to incorporate two-equation turbulence modeling to include turbulence quantities (kinetic energy and length scales) for separated regions.

Flow Solutions

The code was applied to a single-stage-to-orbit hypersonic vehicle that exhibits configuration shape and aerodynamics that are representative of these vehicles. The nose cap of the vehicle is non-spherical and the fuselage has a non-circular cross-section. The fuselage nose leading edge bluntness of the configuration is approximately 1 percent of the local body width at the nose, but rapidly grows to 2 to 3 percent of local body width by 10 percent of body length. This compare to 'blunt' leading-edge wing calculations [4] having a nose radius of 0.7% chord over the entire leading edge. The code was run at Mach numbers from 0.6 to 2.0. Full-configuration calculations were made using a relatively coarse grid (ξ=81, η=30, ζ=165).

Additionally, at one Mach/α condition (Mach=0.6, α=12 degrees), a portion of the forebody to approximately the 55% body length station was run using a finer radial mesh of 74 points. Both the Euler equations and alternatively the full Navier-Stokes equations were solved on this grid, for comparison with the coarse grid results in the nose and forebody region of interest. The Reynolds number used for the viscous calculations was 2.7 X 10^6 per foot. Convergence histories for representative conditions are shown in Figure 1. The effect of increased grid density in the Euler calculations was to decrease convergence rate, as would be expected. The effect of employing the viscous terms was to induce oscillations in the residual, and decrease convergence rate for the higher iterations.

Upper-Surface Flowfield Near Nose

The effect of viscosity and grid density will be illustrated for three data planes in the first 10 percent of the body length. This region is still relatively sharp. The grid topology in the nose region is shown for defined azimuth angles of ϕ=0, 45 and 90 degrees in the schematic of the upper-body region in Figure 2. The upper flowfield above the surface from the centerline to the leading edge is included. The grid dimensions are normalized by the local ray line from the upper centerline to the leading edge and span as:

$$y' = \sqrt{(x^2 + y^2)}$$

For the majority of the Euler calculations, the 'coarse' grid having 30 radial points was used. Cross-plane plots at the three ζ-planes are shown in Figure 3. In these and the following plots, the flowfield above the body is shown from the upper centerline to the leading edge, with a small part of the flowfield ahead of the leading edge ($y'/b_{local}>1$). The geometry presented is limited to the upper surface, but is sufficient to demonstrate the flow features. The 'fine' grid of 74 radial points is shown in Figure 4. The details of the flow structure are shown for the condition Mach=0.6, angle of attack=12 degrees in Figures 5 through 11. Isolines of the pressure coefficient (Figures 5 through 7) show the Euler data are much more overexpanded on the nose centerline (ϕ=0, bottom of figures) than the Navier-Stokes solution. In the fine grid Euler results (Figure 6) the pressures are displaced aft. At a ϕ of 45 degrees (middle of figures), the Navier-Stokes result begins to develop the vortex

structure. The Euler data have local pockets of large suction. At 90 degrees (top of figures), the Euler data have significantly higher suction than the Navier-Stokes results. However, the isolines of the most intense suction lie above the surface. The Navier-Stokes results show a more modest level of suction which reaches the surface in a broad region of the fuselage.

The normalized entropy contours are shown in Figures 8-9. The Euler results on the centerline (bottom of Figure 8) show the large entropy production due to shocks. The high-entropy region follows the leading edge to the ϕ=90 position (top of Figure 8), where substantial entropy gradients still exist near the rotational core. The entropy gradients in the Navier-Stokes solution are much more diffuse (Figure 9.) Since static temperature gradients are greatly reduced in the shockless viscous flow, and pressure changes are more gradual (Figure 7), the magnitude of entropy rise [9]:

$$\frac{(S_2 - S_1)}{c_p} = ln\left(\frac{T_2}{T_1}\right) - Rln\left(\frac{P_2}{P_1}\right)$$

is reduced substantially in the viscous flow at ϕ=90.

The source of the entropy rise in the Euler calculations is the large acceleration required to maintain attached flow. The Mach number profiles for the fine grid are shown in Figure 10. A large zone of supersonic flow lies close to the surface at the centerline, with peak Mach numbers of 1.5. The viscous results (not shown) had no evidence of supersonic flow.

The data for swirl for the three calculations are shown in Figure 11 at a ϕ of 90 degrees. The swirl, or helicity is defined as [10]:

$$H = \overline{V} \cdot \nabla \times \overline{V}$$

Helicity indicates the rotational speed and downstream convection of the vorticity, as well as indicating the rotation sense to pick out primary and secondary structures. The swirl is larger in the Euler results, with 'no' secondary separation region. The peak rotational feature lies closer to the leading edge and down from the viscous result which is much more diffuse. The fine grid provides much improvement in resolution of the Euler results. A negative swirl region at the left of the ϕ=90 view is eliminated through grid refinement. The rotational structures in the solutions for this relatively flat nose appear driven by leading-edge effects, rather than the forebody crossflow separation effects of References 5-7.

We can relate entropy gradients to vorticity through the Second Law of Thermodynamics and the equation of motion [11]:

$$T\nabla s = \overline{V} \times \nabla \times \overline{V}$$

We decompose the right-hand side yielding:

$$\left[v(\omega_z) - w(\omega_y)\right]_i$$

$$\left[u(\omega_z) - w(\omega_x)\right]_j$$

$$\left[u(\omega_y) - v(\omega_x)\right]_k$$

Large entropy gradients are created in the Euler solution around the nose. Since the v-and w- velocity components are zero on the centerline, at ϕ=0 the entropy gradients are convected only in the j-term in which w_z contains spanwise velocity gradients. As ϕ is increased to 90 degrees, contributions from v and w increase. Therefore, the vorticity will be convected from the centerline to the axial downstream planes.

Vortex Lift Comparisons with Experiment

The integrated forebody pressure forces are shown in Table 1 and are normalized by subsonic wind tunnel

Table 1: Normalized Integrated Forces Over Forward 55% of Fuselage at Mach=0.6, α=12

Solver	Grid ξ, η, ζ	C_L/C_{Lref}	C_M/C_{Mref}	C_D/C_{Dref}
Euler	81, 30, 66	0.498	5.370	0.082
Euler	81, 74, 66	0.490	4.722	0.011
Navier-Stokes	81, 74, 66	0.492	4.476	0.032

test data for the full configuration. The large magnitude of the pitching moment terms in the normalized data are caused by a small reference pitching moment (caused by the nozzle afterbody influence). The pitching moment and drag show that grid refinement brings the Euler results closer to the viscous-calculated results.

An estimate of vorticity-induced suction was made by assigning pressure less than 92% of a nominal attached-flow level (near the upper centerline at the given ζ plane) as being vortex-induced. The amount of affected area of the upper surface was surveyed, and the incremental normal force due to this additional suction were calculated. The results are shown in Table 2, normalized by the normal force produced by the entire upper surface area. Although the area of

Table 2: Affected Area and 'Vorticity C_N'

Solver	Grid ξ, η, ζ	% Area	% upper-surface C_N due to vorticity
Euler	81, 30, 66	4.8%	26.8%
Euler	81, 74, 66	5.5%	38.8%
Navier-Stokes	81, 74, 66	5.6%	20.6%

vortex-induced pressure is similar between the Euler results and the viscous results, the percentage of lift from the forebody vortex is higher in the Euler results. This is due to the more-intense vorticity near the nose, and increased amount of local suction. As seen in the pressure distributions in Figure 5 and 6, the fine-grid Euler solution creates larger suction pressures at ϕ=90 (due to non-physical overexpansion under the rotational structure) and thus compares poorly to the viscous 'vorticity C_N' result. The Euler predictions of total forebody pitching moment and pressure drag (Table 1) are improved with refinement, showing a pitfall of using only total quantities for grid studies.

The full-vehicle forces were calculated for the coarse-grid Euler calculations. The variation between the Euler-predicted integrated surface pressure forces and test data is shown in Figure 12. Overall agreement is good for lift. The coarse grid has difficulty resolving pitching moment. The fine-grid results from Table 1 indicate that better resolution improves the prediction. The pressure drag was found to be underpredicted. Flowfield integrations of x- and z- momentum were made at the back plane of the computational solution to check the drag results. The trend of momentum deficit versus angle of attack at the backplane agreed with the trend of drag from surface pressure integration. The magnitude of this wake drag was underpredicted by a constant amount from the surface integrated pressure drag. This indicates that flow turning ahead of the backplane increases the overall momentum level at the rear of the computational domain. Outer boundary integrations should consider the size and geometry of the domain.

Conclusions

For the given non-spherical nose configuration, the predicted flowfield was more in character with wing leading-edge separation than forebody separation. The Euler solutions were characterized by large amounts of vorticity generated by entropy gradients at the centerline which appeared to be convected around the leading edge. The upper-surface rotational flow appeared to be generated by overexpansion as in previous studies. By contrast, the Navier-Stokes result showed the vortical development occurring farther aft. The integrated forces from the Euler predictions compared well with test data, for the relatively fine grid. However, local flow quantities such as cross-flow shocks, position of rotational features, extent of overexpansion regions, and 'vorticity-induced' normal force were mis-predicted and were at times adversely affected by grid refinement. This suggests that grid-refinement studies for Euler solvers should survey all relevant flow parameters.

References

1. Hartwich, P.M., and Hall, R.M., "Navier-Stokes Solutions for Vortical Flows over a Tangent-Ogive Cylinder," *AIAA Journal*, Vol. 28, July 1990, pp. 1171-1179.

2. McMillin, S.N., Thomas, J.L., and Murman, E.M., "Euler and Navier-Stokes Leeside Flows over Supersonic Delta Wings," *Journal of Aircraft*, Vol. 26, May 1989, pp. 452-458.

3. Hicks, R., etal, "Euler and Potential Computational Results for Selected Aerodynamic Configurations," *Progress in Astronautics and Aeronautics: Applied Computational Aerodynamics*, P.A. Henne, Editor, Vol. 125, AIAA, Washington, D.C., 1990, pp 263-290.

4. Rizzi, A., and Muller, B., "Vortex Flow Modelling with Euler and Navier-Stokes Equations," *Numerical Methods in Fluid Dynamics.*

5. Hartwich, P.M., Hall, R.M., and Hemsch, M.J., "Navier-Stokes Computations of Vortex Asymmetries Controlled by Small Surface Imperfections," *Journal of Spacecraft and Rockets*, Vol. 28, March-April 1991, pp. 258-264.

6. Schiff, L., Degani, D., and Cummings, R.M., "Computation of Three-Dimensional Turbulent Vortical Flows on Bodies at High Incidence," *Journal of Aircraft*, Vol. 28, Nov. 1991, pp. 689-699.

7. Hartwich, P.M., and Hall, R.M., "Symmetry-Breaking in Vortical Flows Over Cones-Theory and Numerical Experiments," AIAA Paper 93-3408-CP, August 1993.

8. Cooper, G.K., "The PARC Code: Theory and Usage,", AEDC-TR-87-24, October 1987.

9. White, F.M., *Viscous Fluid Flow*, McGraw-Hill, New York, 1974, p. 199.

10. Levy, Y., Seginer, A. and Degani, D., "Graphical Representation of Three-Dimensional Vortical Flows by Means of Helicity Density and Normalized Helicity," AIAA Paper 88-2598, June 1988.

11. Landau, L.D. and Lifshitz, E.M., *Fluid Mechanics*, Pergamon Press, London, 1959, pg 5.

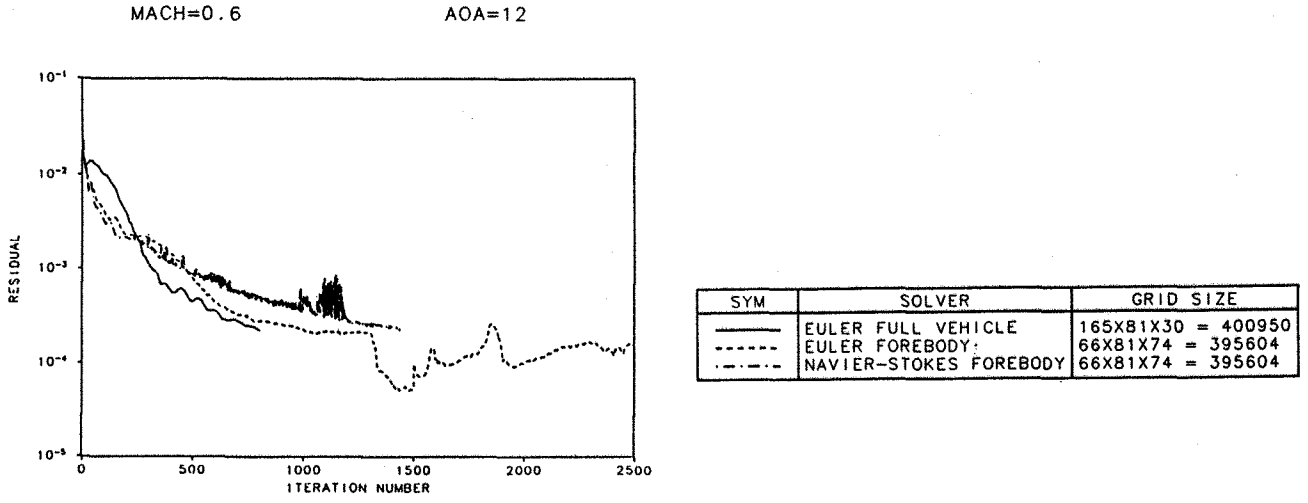

Figure 1. Convergence History for Hawk3D Calculations

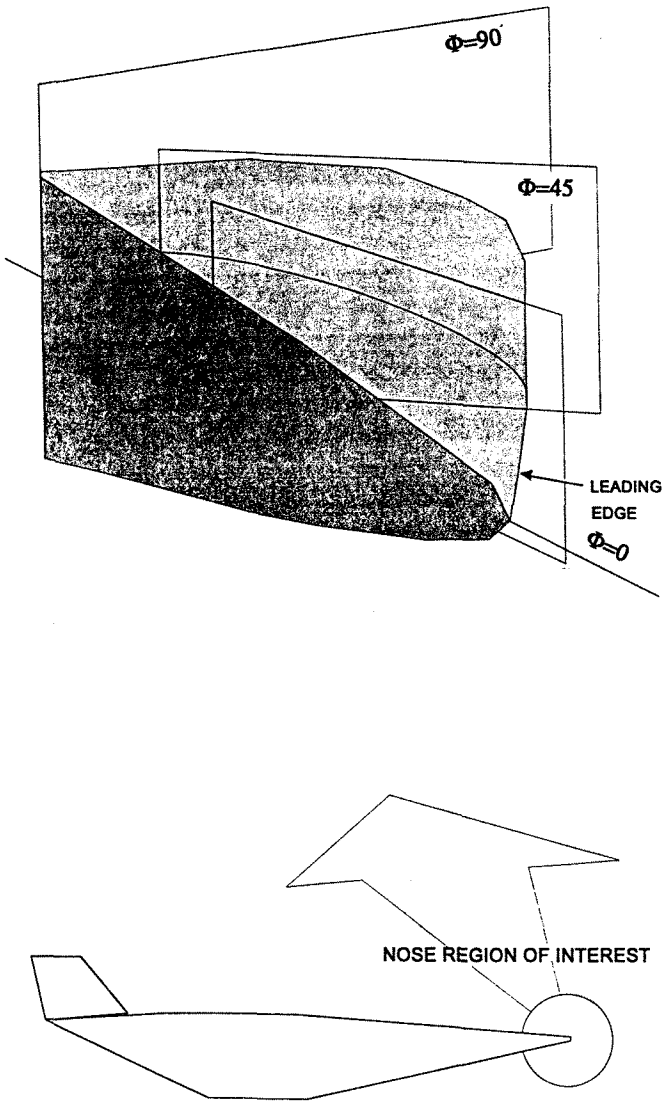

Figure 2. Geometry of Flowfield Views in Nose Region

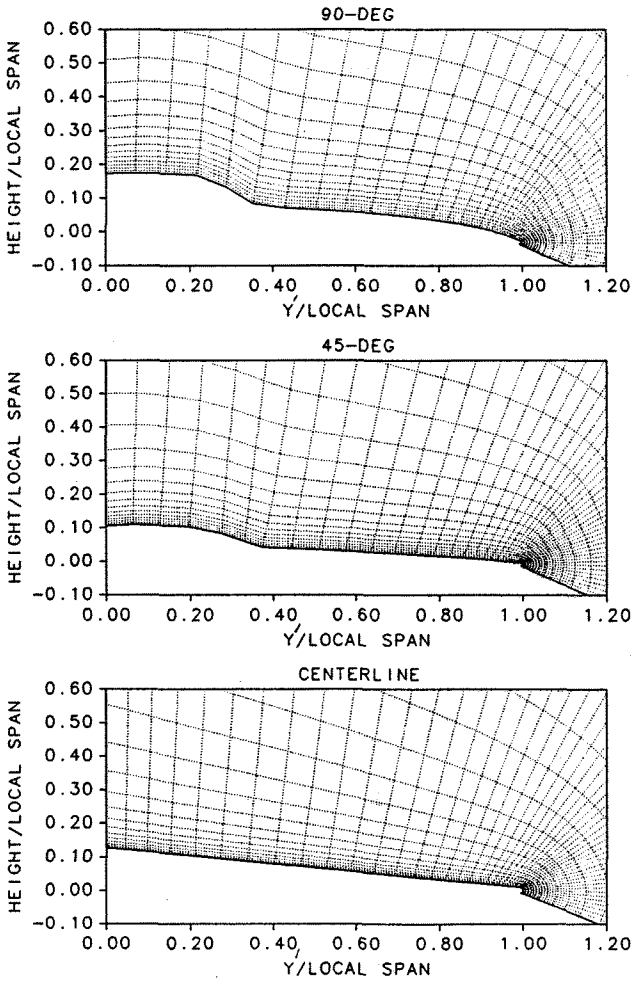

Figure 3. Geometry of Euler Coarse Grid in Upper-Surface Region

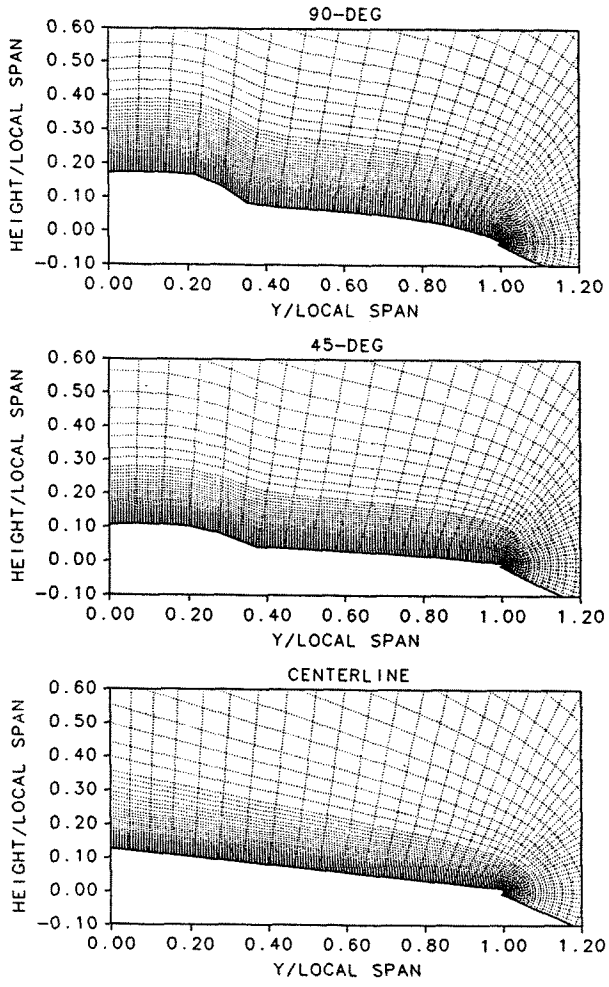

Figure 4. Geometry of Fine Grids for Euler and Navier-Stokes Calculations

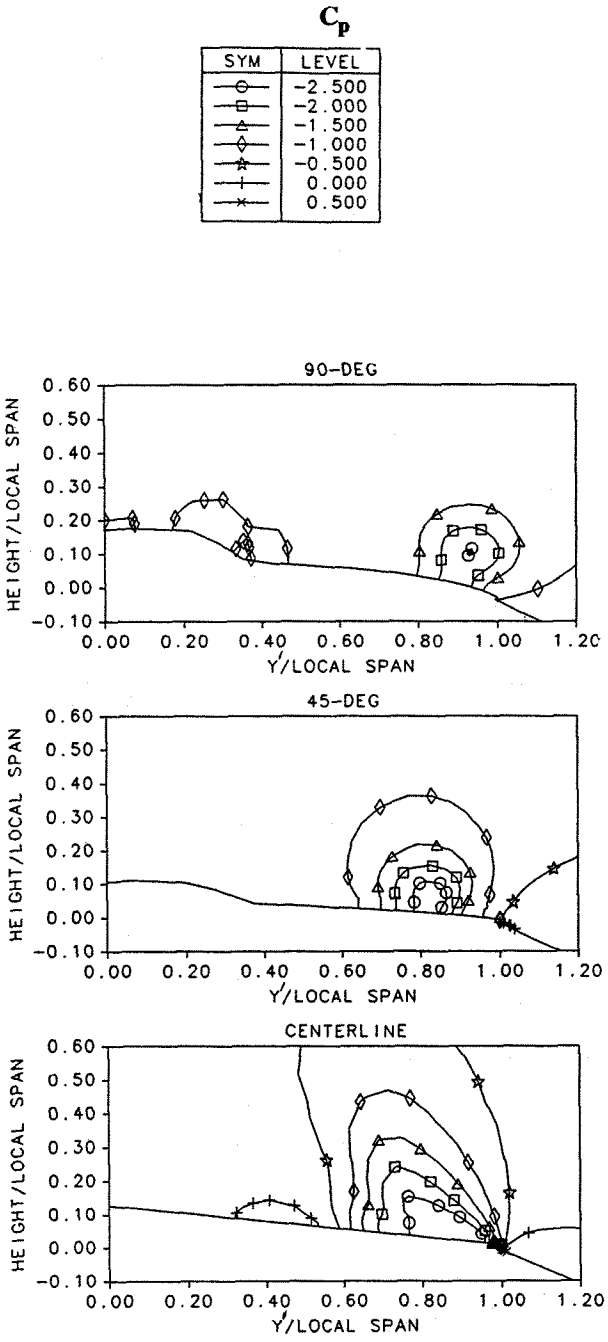

Figure 5. Pressure Coefficient using Coarse Grid and Euler equations

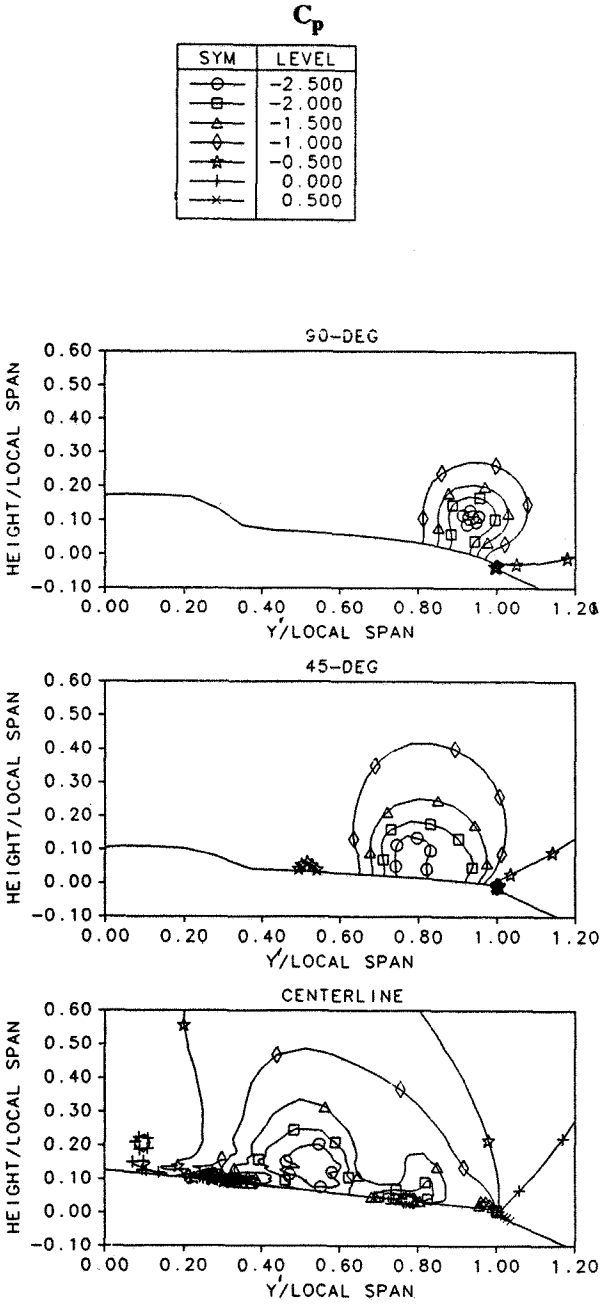

Figure 6. Pressure Coefficient using Fine Grid and Euler equations

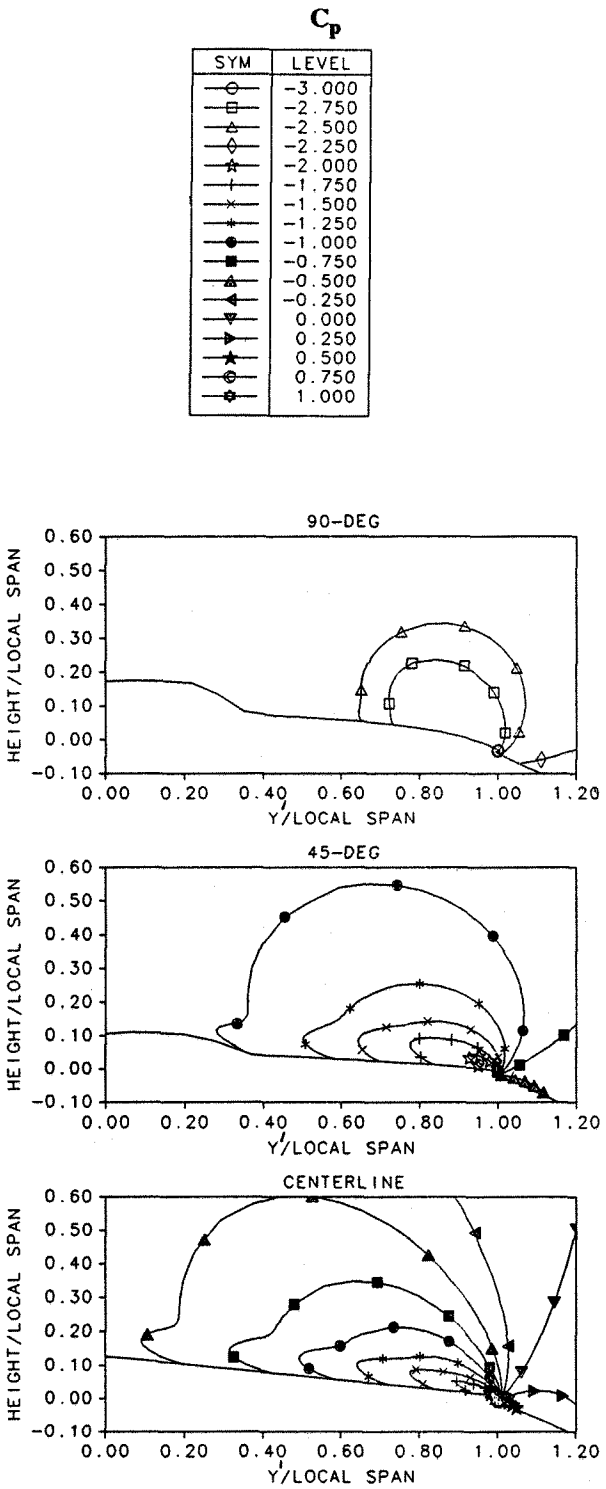

Figure 7. Pressure Coefficient using Fine Grid and Navier-Stokes equations

Note: Entropy has been normalized by maximum value

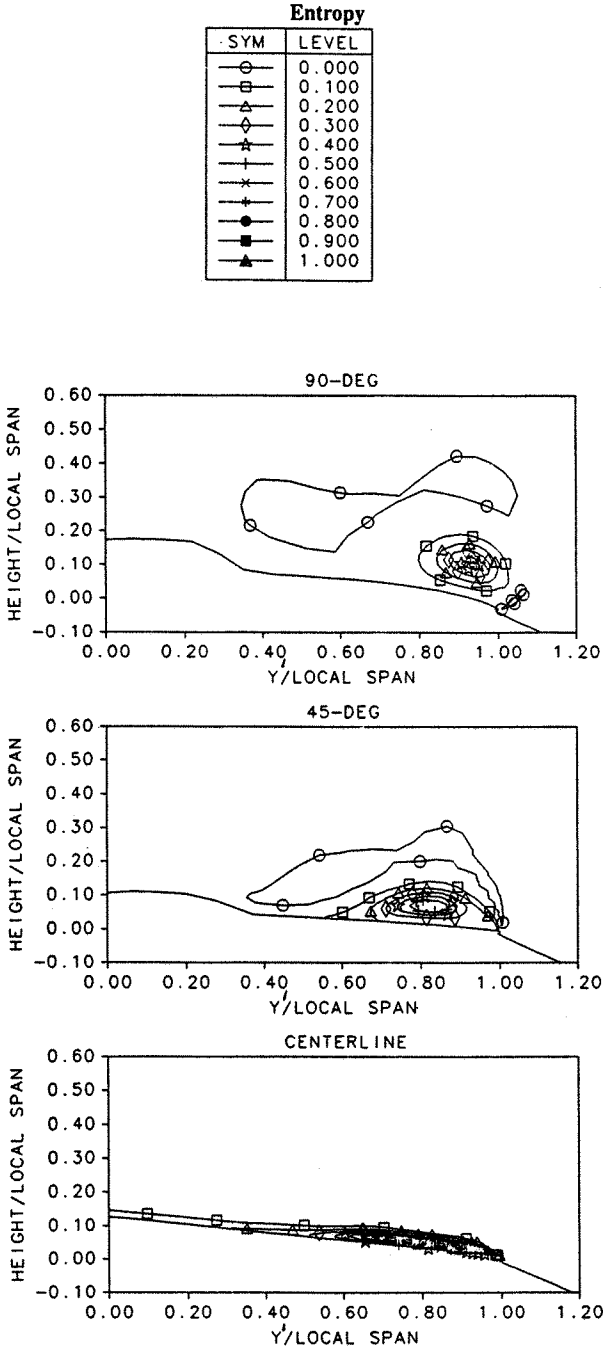

Figure 8. Entropy Contours using Coarse Grid and Euler equations

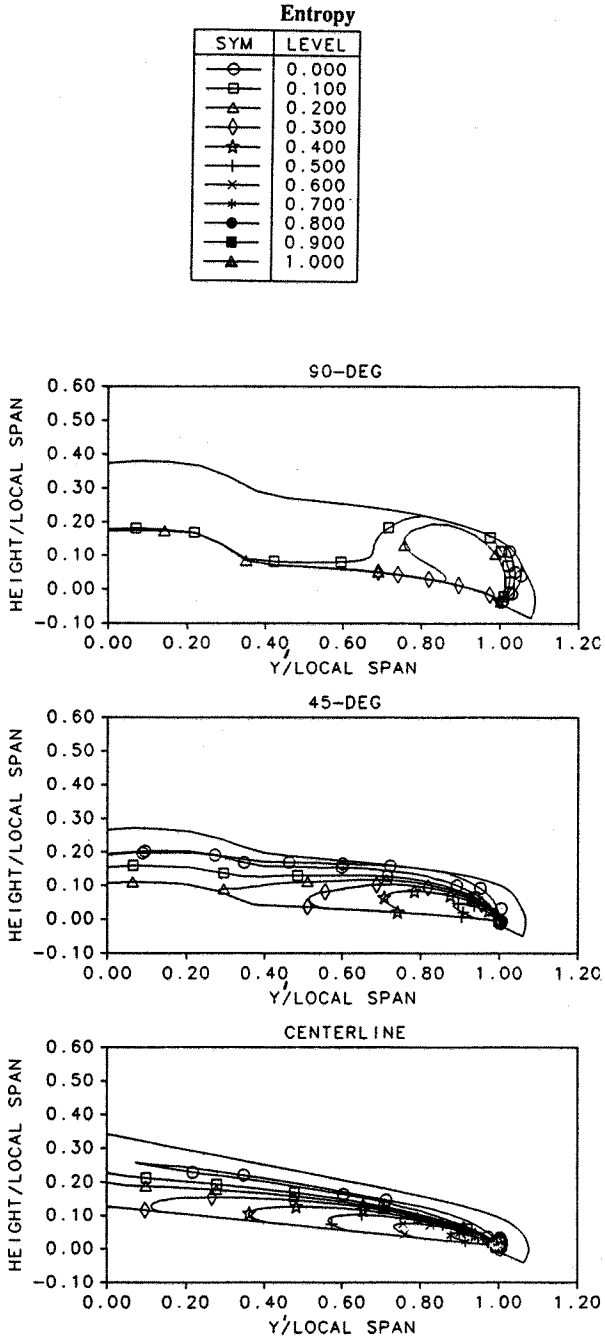

Figure 9. Entropy Contours using Fine Grid and Navier-Stokes equations

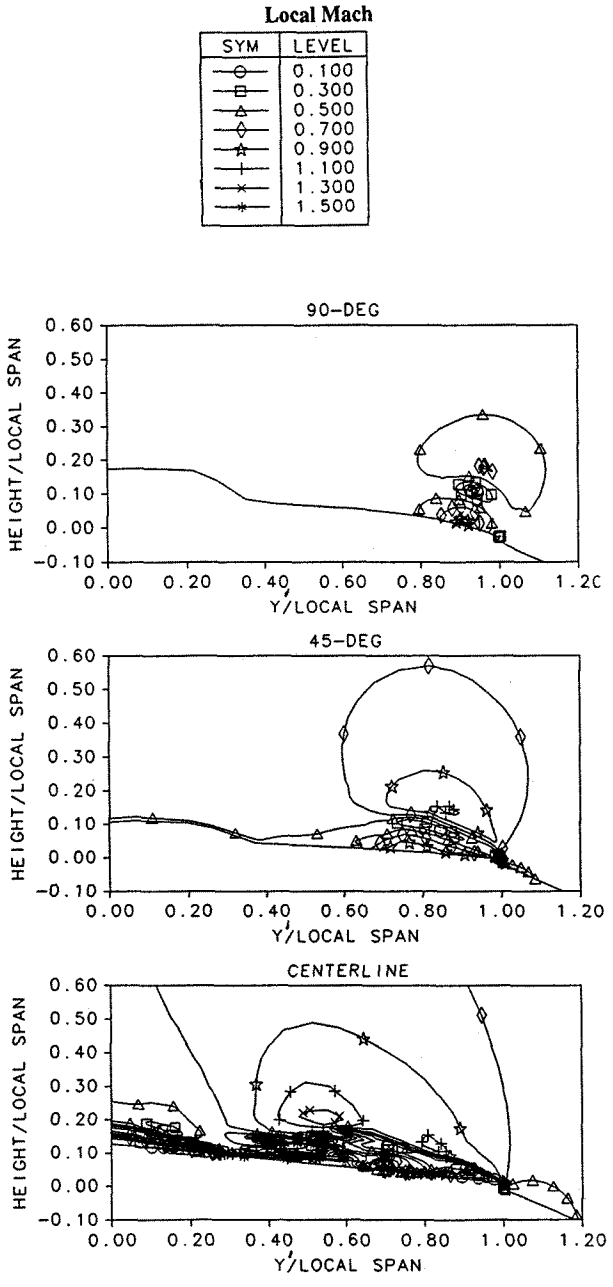

Figure 10. Local Mach Number using Fine Grid and Euler equations

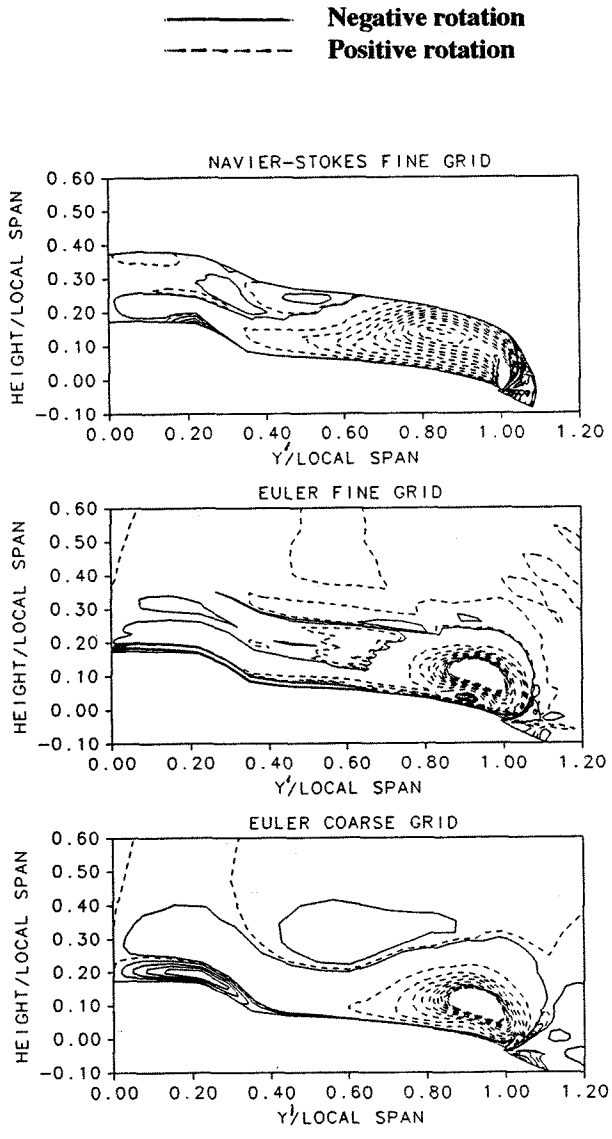

Figure 11. Helicity Density at ϕ=90 degree Plane for Three Solutions

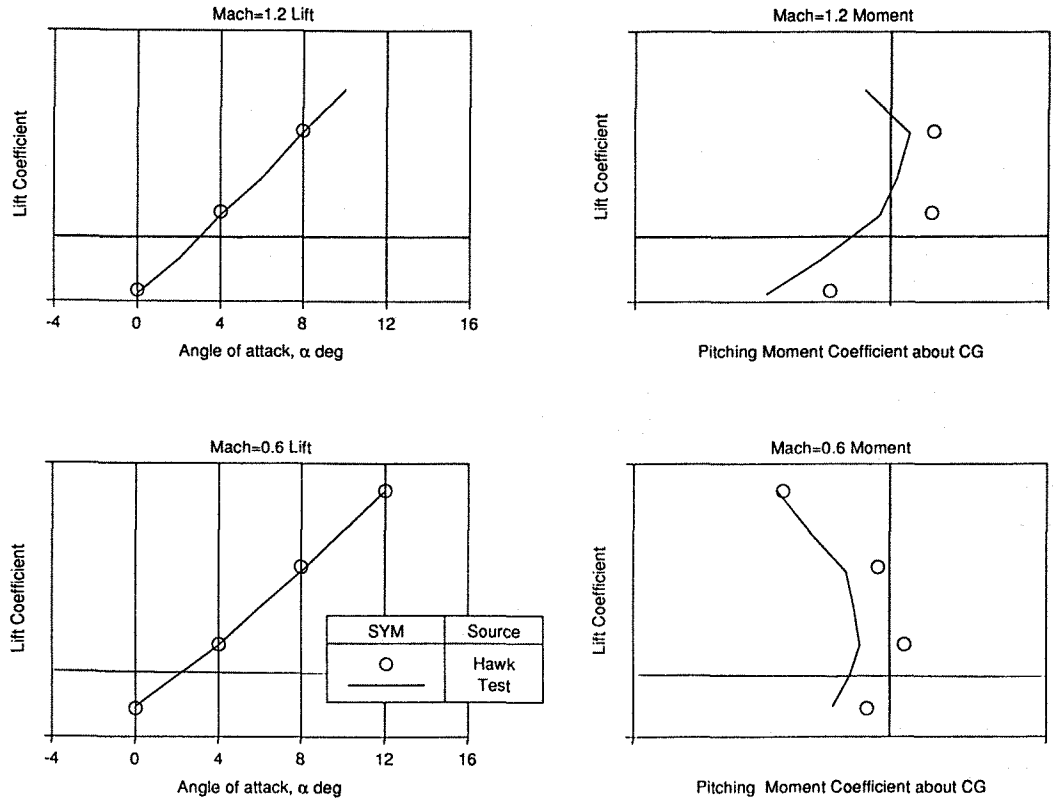

Figure 12. Comparison of Force and Moment Predictions to Test Data